

Explainable Machine Learning Identification of Superconductivity from Single-Particle Spectral Functions

Xu Chen,^{1,*} Yuanjie Sun,^{2,*} Eugen Hruska,¹ Vivek Dixit,² Jinming Yang,³ Yu He,^{4,†} Yao Wang,^{1,2,‡} and Fang Liu^{1,§}

¹*Department of Chemistry, Emory University, Atlanta, GA 30322, United States*

²*Department of Physics and Astronomy, Clemson University, Clemson, SC 29631, United States*

³*Department of Physics, Yale University, New Haven CT, 06511, United States*

⁴*Department of Applied Physics, Yale University, New Haven CT, 06511, United States*

(Dated: June 10, 2024)

Abstract: The traditional method of identifying symmetry-breaking phase transitions through the emergence of a single-particle gap encounters significant challenges in quantum materials with strong fluctuations. To address this, we have developed a data-driven approach using a domain-adversarial neural network trained on simulated spectra of cuprates. This model compensates for the scarcity of experimental data – a significant barrier to the wide deployment of machine learning in physical research – by leveraging the abundance of theoretically simulated data. When applied to unlabeled experimental spectra, our model successfully distinguishes the true superconducting states from gapped fluctuating states, without the need for fine temperature sampling across the transition. Further, the explanation of our machine learning model reveals the crucial role of the Fermi-surface spectral intensity even in gapped states. It paves the way for robust and direct spectroscopic identification of fluctuating orders, particularly in low-dimensional, strongly correlated materials.

Understanding and controlling the materials' physical properties are key pursuits of the quantum materials research today. Since the electronic structure of materials underpins many physical properties, the single-particle spectral function proves to be an effective quantity for their characterization [1]. This function captures the probability of an individual electron occupying a specific energy-momentum state in a many-electron system. While it cannot replace the full many-body wavefunction, it provides insights into the low-energy properties such as conductivity and thermal excitations. Notably, the single-particle spectral function can be directly measured using angle-resolved photoemission spectroscopy (ARPES). Both lab-based and synchrotron-based ARPES techniques have been extensively employed to investigate emergent electronic states in materials [2, 3], substantially accelerating the advancement in the field of quantum materials [4].

As investigations into quantum materials deepen, new challenges arise due to the inherent limitations of representing a many-body state with only its single-particle excitations. For traditional metals and semiconductors, this approximation is effective as interactions are sufficiently screened. In such scenarios, ARPES can accurately identify electronic phase transitions through a single-particle gap, stemming from the development of a (mean-field) order parameter. By measuring the energy gap size, one can deduce the strength of order parameters. However, in quantum materials, emergent phases are substantially influenced, or even governed, by entanglement among multiple particles. Consequently,

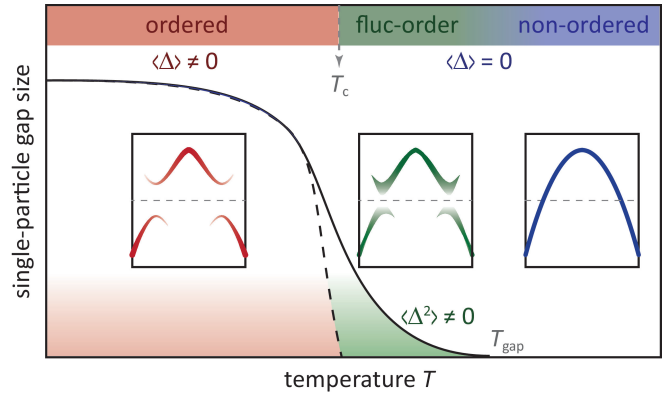


FIG. 1. Schematic illustrating the single-particle gap in materials experiencing strong fluctuations. At low temperatures (red), the material exhibits a nonzero order parameter $\langle \Delta \rangle \neq 0$ and a well-defined single-particle gap. As the temperature increases above T_c (green), the local excitations lose long-range coherence and the average order parameter $\langle \Delta \rangle = 0$. However, the system still displays pronounced fluctuations with a non-negligible $\langle \Delta^2 \rangle$, leading to a finite single-particle gap. These short-range fluctuations gradually diminish with further temperature increase, ultimately resulting in a normal state (blue).

these phases often deviate from traditional mean-field theory predictions. For example, transitions between phases with distinct symmetries often lead to a regime characterized by intense short-range fluctuations. The effects of these fluctuations on the single-particle spectral function are similar to that of a broken-symmetry long-range order, often reflected in the form of partial spectral weight depletion that precedes the establishment of a full energy gap (see Fig. 1). This phenomenon has been widely observed in Mott insulators, charge density wave systems, and unconventional superconductors above their thermodynamic phase transition temper-

* X.C. and Y.S. contributed equally to this work.

† yu.he@yale.edu

‡ yao.wang@emory.edu

§ fang.liu@emory.edu

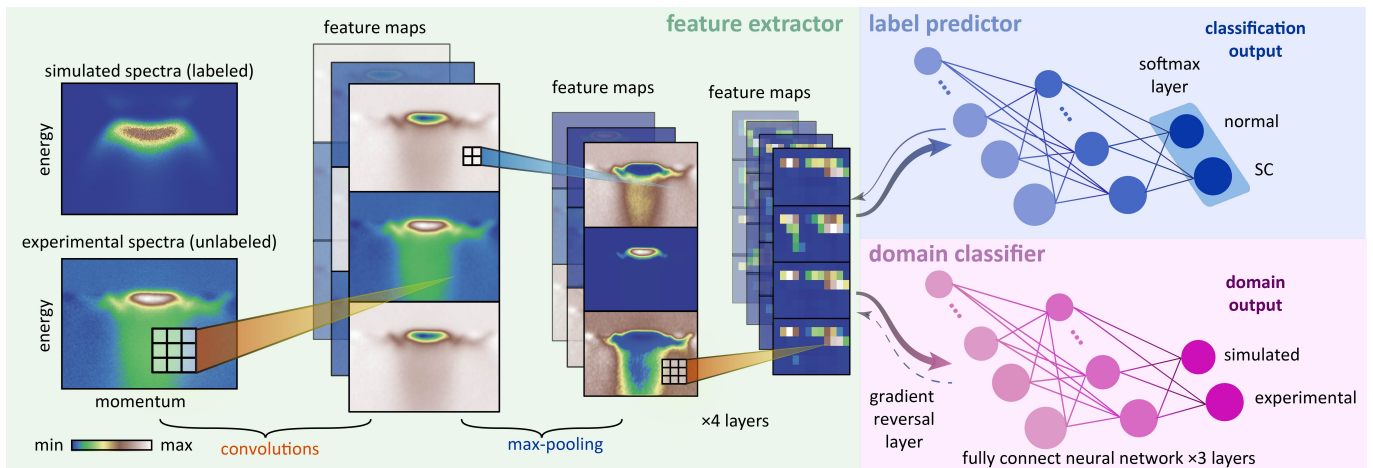


FIG. 2. **Model architecture.** Left to right: Consecutive convolutional stacks as the feature extractor convert the ARPES spectrum (using experimental data for BSCCO OD58 as an example) into feature maps with various convolutional kernels. A pooling layer and activation are then applied to compress the feature maps and pass the data to the next layer. After four convolutional layers, the feature maps are pooled and flattened, then directed into two distinct fully connected neural networks: The label predictor (blue) classifies the spectra into the superconducting (SC) and normal phases; The domain classifier (pink) classifies the sample source either from simulation or experiment. It connects to the feature extractor via a gradient reversal layer that multiplies the gradient by a certain negative constant during the backpropagation (dashed line). The number and size of each layer plotted in this figure are for illustrative purposes.

atures [5–9]. This often renders spectroscopic probes incapable of detecting thermodynamic phase transitions, despite the rapidly growing demand for *in situ* and *in operando* detection of novel electronic phases [10, 11].

Superconductivity stands out as a central topic in condensed matter research, characterized by dissipationless transport due to the formation of global phase coherence among Cooper pairs of electrons. In the mean-field framework, superconductivity is linked to a single-particle gap twice the size of the order parameter. In scenarios where direct transport measurements are impractical – such as with thin films, functionalized surfaces, nonequilibrium systems, or extreme conditions precluding direct contacts – the presence of this gap serves as a fingerprint of superconductivity [12–14]. However, in correlated materials like cuprates and FeSe, quantum fluctuations disrupt the direct link between the gap and superconductivity [5–8]. In these cases, the gap-opening temperature T_{gap} can significantly exceed the superconductivity transition temperature T_c . There is a pressing need for an efficient approach to directly identify superconductivity from the single-particle spectra alone, to facilitate high-throughput discovery of superconductive materials. Recent studies have revealed the potential for ARPES to also encode information on superconducting phase coherence [8, 15, 16], but pinpointing this information remains challenging without tracking the full temperature evolution of quasiparticle intensity. This challenge likely stems from the oversimplification of the highly complex spectra of a many-body system.

To address this issue, we develop a machine learning (ML) model to directly classify ordered superconducting phases from ARPES spectra without needing complete

temperature-dependent trends. One significant challenge we face is the limited experimental training data, a ubiquitous obstacle in artificial intelligence (AI) for science community [17]. While most state-of-the-art ML algorithms are data demanding, scientific data such as ARPES spectra are often scarce due to the complexity of experiments and the lack of standardization in data curation. A promising solution is to utilize training data curated in a simulated environment to enable efficient exploration of the parameter space *in silico* [18]. Inspired by this idea, we train a convolutional neural network (CNN) model using simulated ARPES spectra and then apply it to classify experimental ARPES spectra. CNN is chosen here due to its wide applications in image classification, where filters in convolutional layers distill specific patterns from two-dimensional data. However, the idealized conditions assumed in simulations often fail to replicate the experimental noise, resolutions, and laboratory condition variability, leading to poor performance when applying simulation-trained models to actual experimental data. To overcome this experiment-simulation discrepancy, we employ domain adaptation techniques to adversarially train the CNN.

As illustrated in Fig. 2, the domain adversarial neural network (DANN) [19] adapted in this work comprises a feature extractor, a domain classifier, and a label predictor. The feature extractor extracts a shared feature representation of both simulated and experimental spectra. The domain classifier then determines whether the extracted features originate from the simulated or experimental datasets. The label predictor utilizes these features and outputs the corresponding material sample’s phase label, which can be either superconducting (SC) or

normal phase. Unlike traditional CNN, which comprises only a feature extractor and a label predictor, the domain classifier discourages the feature extractor from generating distinguishable representations between simulated and experimental data. This setup promotes the emergence of latent representations that are shared by both simulated and experimental spectra during optimization. Importantly, the label predictor is trained exclusively on the labeled simulation data (SC vs normal), with no phase information required for the experimental spectra. Thus, the model is transferable to classify experimental spectra at any random temperature. To enable phase label prediction, a softmax layer is added to the label predictor to convert the predicted logits μ_α for each phase α ($\alpha = \text{SC}$ or normal) into probability values $p_\alpha \propto e^{\mu_\alpha}$, obeying the sum rule $\sum_\alpha p_\alpha = 1$.

The experimental ARPES spectra were collected for two cuprate samples: a super-oxygenated $\text{Bi}_2\text{Sr}_2\text{CaCu}_2\text{O}_8$ (BSCCO) with $T_c = 50$ K (OD50) and an oxygenated BSCCO with $T_c = 58$ K (OD58). A total of 41 and 45 spectra are measured in these two samples, respectively, spanning over a wide temperature range from 14 K to 102 K and both superconducting and normal phases (reused from Refs. 20 and 8). To better distinguish fluctuations encoded in spectral features, we applied a uniform background removal approach to both simulated and experimental data (see Supplementary Note 1). Fig. 3a presents four spectra taken from the OD50 sample after the background removal. While superconductivity, determined by transport measurements, disappears when the temperature exceeds 50 K, the single-particle gap remains open until $T_{\text{gap}} = 65$ K [20]. It is important to note that the true label, or the phase corresponding to each experimental spectrum, is invisible to our ML model. All labeled training data are obtained from simulations following the method outlined in Ref. 8 (see Methods for details).

Figures 3b and c show the phase classification results for the BSCCO OD50 and OD58 experimental spectra. The model’s predictions are represented by a scalar “SC probability” \bar{p}_{SC} for each input spectrum. Such an SC probability \bar{p}_{SC} is obtained from an ensemble approach, where \bar{p}_{SC} for each spectrum is the averaged p_{SC} over 10 different DANN models with various initializations. Normalized by the sum rule, a sample corresponding to an input spectrum is predicted as SC when \bar{p}_{SC} exceeds 50%. For the BSCCO OD50 sample, only one spectrum measured in the normal phase is misclassified as SC. Conversely, all other 40 experimental spectra are correctly classified, yielding an accuracy of 97.6%. The performance is similar for the OD58 sample, where only one spectrum in the SC state is misclassified.

As the experimental spectra are obtained for two material samples at different temperatures, we further analyze the predicted SC probability \bar{p}_{SC} as a function of temperature in Figs. 3c and d. Although our ML model independently classifies each ARPES spectrum and does not have access to temperature information, we

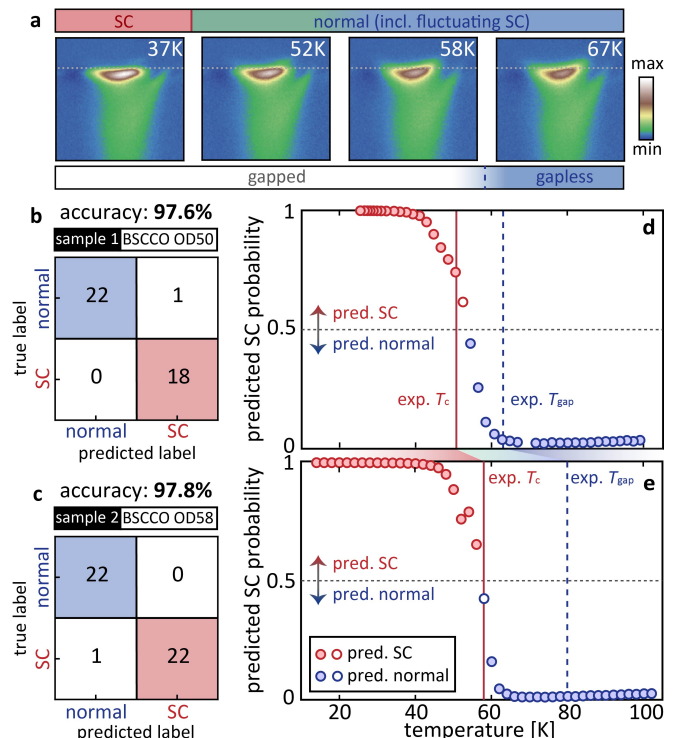


FIG. 3. Classification of superconducting phase using the DANN model. **a** Experimental ARPES spectra for the BSCCO OD50 sample at four different temperatures, with dashed lines denoting the Fermi level. The upper and lower bars indicate the phase labels, independently determined by experiments and invisible to the ML model, and the gap sizes. **b,c** Confusion matrices obtained for binary classification of the ARPES spectra collected from **b** BSCCO OD50 and **c** OD58 samples at various temperatures, yielding accuracies of 97.6% and 97.8%, respectively. **d,e** The ML-predicted SC probability \bar{p}_{SC} for spectra obtained from the **d** BSCCO OD50 and **e** OD58 samples, respectively. The \bar{p}_{SC} s are calculated for each spectrum but are sorted here by their experimental temperatures, which are unknown to the ML model. The classification is based on whether \bar{p}_{SC} exceeds 0.5. Correctly classified spectra are denoted by solid red and blue dots, while misclassified data are depicted by open dots. The red and blue lines indicate experimentally determined transition temperature T_c and gap-opening temperature T_{gap} (both invisible to the ML model), respectively.

observe a roughly monotonic relationship between \bar{p}_{SC} and the actual temperature T . The overall shape of the $\bar{p}_{\text{SC}}(T)$ resembles an inverted sigmoid function: it shows constantly high values (close to 1) at low T and low values (close to 0) at high T , with a rapid transition from 1 to 0 near the experimentally determined T_c . The only misclassified data point in Fig. 3c corresponds to a sample measured at a temperature close to T_c . Given that none of the experimental spectra are labeled in ML, the monotonic decrease in the predicted probability with increasing temperature indicates that our model has successfully captured the superconducting phase ordering encoded in the details of ARPES spectra. Interestingly,

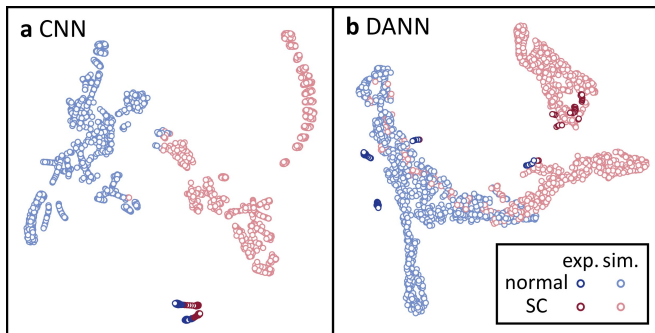


FIG. 4. **t-SNE visualization of feature distributions.** **a** The distribution of the feature extractor’s activations of the CNN model without domain adaptation. **b** The distribution of feature extractor’s activations of the CNN model when the adaptation procedure was incorporated into training. Light blue and red colors indicate the simulated spectra belonging to normal or SC phases, respectively, while dark colors represent experimental spectral data.

the predicted \bar{p}_{SC} does not exhibit any anomaly near the T_{gap} . These observations reflect that the gap opening is not the sole or even primary indicator of phase transition in quantum materials. The spectral details beyond the mere presence of a gap contain extensive information about the underlying phases.

It is worth noting that the simulated and experimental ARPES spectra exhibit fundamental differences, as shown in Fig. 2, due to the simplicity of the single-band model. Thus, the domain adaptation technique is crucial in bridging the gap between the simulated training spectra and experimental test spectra, hence ensuring our ML phase classifier’s high accuracy. Without the adversarial training enabled by the domain classifier, the CNN model yields a representation space where the simulated and experimental spectra occupy distinct regions of the latent space, as visualized by the t-distributed stochastic neighbor embedding [21] (t-SNE) in Fig. 4a. This separation reflects the intrinsic differences between simulated and experimental data. As a result, the classification rules learned from the simulated spectra are not directly applicable to experimental spectra. In contrast, the domain classifier in DANN significantly enhances the alignment between simulated and experimental spectra in the representation space (see Fig. 4b), providing transferable classification rules between simulated and experimental spectra. Consequently, the classification results show a substantial improvement by 19.0% and 19.2% in average accuracy on the BSCCO OD50 and OD58 samples, respectively (see Supplementary Note 2).

Beyond classifying superconductivity from ARPES spectra, we also aim to extract interpretable physical parameters from the ML model to deepen our understanding of quantum materials. Specifically, we seek to identify which single-particle spectral features are linked to the superconductivity long-range order via an occlusion-based analysis for the ML model [22]. This

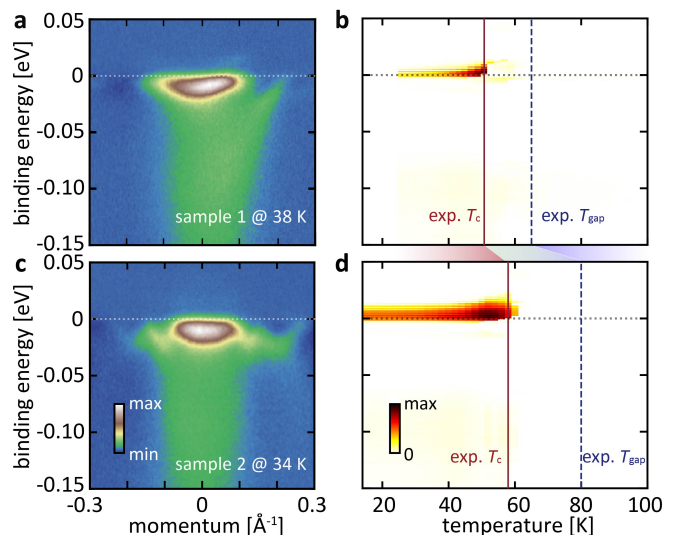


FIG. 5. **Saliency distribution for experimental spectra.** **a** A sample ARPES spectrum obtained from BSCCO OD50 at 38 K (superconducting phase). **b** The saliency values across various binding energies and temperatures for the BSCCO OD50 sample, quantifying the sensitivity of the ML prediction for each energy. **c** An ARPES spectrum from BSCCO OD58 at 34 K (superconducting phase). **d** Saliency values for the BSCCO OD58 sample. Grey dashed lines denote the Fermi level, while red and blue lines indicate the T_c and T_{gap} , as independently determined by experiments.

analysis measures the significance of specific portions of an ARPES spectrum to the model’s classification decision by assessing the saliency, defined as Eq. (9) in **Methods**. We analyze saliency for each individual energy level, which reflects the change in the phase prediction, in terms of \bar{p}_{SC} when an entire row of the spectrum is obscured or occluded.

As shown in Fig. 5, we obtain the saliency as a function of binding energy for each spectrum in both BSCCO OD50 and OD58 experimental datasets. A notable feature across various spectral samples is a pronounced peak at $\omega = 0$. Remarkably, the saliency magnitude significantly decreases for spectra acquired at temperatures above T_c . This observation suggests that the ML model identifies the nuanced distribution of spectral weight near and above the gap center as the key for pinpointing the true T_c . The spectral weight just above the gap center is particularly sensitive to the upper branch formation of the Bogoliubov quasiparticles, whose clear separation from the lower branch is a major empirical identifier of superconducting phase ordering in cuprates [8]. In an intriguing parallel, a recent study inferred electronic entropy from a continuous sequence of ARPES spectra, achieved through meticulous temperature and energy calibration [15]. This study deduced that the temperature-derivative of weighted spectral intensity near $\omega = 0$ could effectively determine the T_c . Our ML model’s explanation aligns with this conclusion. However, different from the temperature-derivative ap-

proach, the ML classification and the saliency analysis operate on each individual ARPES snapshot, without relying on temperature and phase information. The experimental data, used solely for domain alignment, remain unlabeled. This approach of unsorted-snapshot-based classification approach is particularly valuable for general material design, where precise parameter tuning and sequential measurements are impractical, such as under extreme or non-equilibrium conditions.

Recalling the original motivation for this spectrum-based phase classification, we must particularly investigate the fluctuating superconducting (fluc-SC) regime in the normal state. This regime is characterized by prominent short-range Cooper pair fluctuations and the single-particle gap comparable to that observed below T_c [5–8]. To further assess the robustness of our model, we expand the classification to include three states: SC, fluc-SC, and gapless non-SC states. As detailed in Supplementary Note 3, the spectra stemming from SC and gapless non-SC states are still correctly classified under this ternary classification. However, distinguishing the fluc-SC phase proves challenging, resulting in an overall accuracy of 85.4% and 75.6% for BSCCO OD50 and OD58 samples, respectively. Despite the reduced accuracy, domain adaptation remains crucial in the ternary classification. The domain classifier in DANN improves the accuracy compared to traditional CNN by more than 10% and 30% with (Supplementary Table 1) and without (Supplementary Table 2) the ensemble average, respectively. An interesting observation is that the majority (15 out of 17) of (gapped) fluc-SC states are misclassified as gapless non-SC states. This misclassification occurs regardless of the gap, which was typically read by APRES at first glance and regarded as a fingerprint for long-range orders. Instead, our ternary classification results indicate that traditional single-particle spectroscopy interpretations may oversimplify the complexities inherent in quantum materials. Distinguishing the gapped fluc-SC state from the gapless non-SC state is more challenging than distinguishing between the equally gapped SC and fluc-SC states. This outcome also indicates that the ML model correctly recognizes the intrinsic similarities between fluc-SC and non-SC states, as both belong to the normal phase of these materials.

In summary, this study demonstrates that a transferable ML model trained without labeled experimental data can successfully classify the superconductivity of quantum materials based on real experimental ARPES spectra. This achievement paves the way for using single-particle spectra to identify long-range orders, even when the deterministic features do not conform to traditional gap analysis. The transferability of our model is demonstrated by its application to ARPES spectral datasets collected from two materials with distinct compositions measured at various temperatures. The snapshot-based classification without the need to track temperature-dependent trends enables high-throughput characterization of superconductivity in correlated materials, with

potential in pump-probe spectra where phases lose coherence [23–25]. Furthermore, the physical intuition extracted from the ML model using the occlusion-based explanation method aligns well with domain knowledge. Our approach fits within the growing emphasis on transfer learning [26, 27] and domain adaptation techniques [28, 29] in scientific applications to overcome data scarcity. Despite the challenges compared to existing efforts (fewer available experimental data, a larger discrepancy between simulation and experiment, and more complicated underlying patterns), our model achieves satisfactory performance in classifying superconductivity in quantum materials, thereby enabling high-throughput material design and synthesis experiments that require immediate characterizations [30].

METHODS

A. Simulated ARPES Data

ARPES data simulation is primarily based on the phenomenological model described in Ref. 8. The superconducting pairing onset temperature T_{gap} is determined by the gap opening temperature, and the thermodynamic transition temperature T_c is determined by the steepest change of quasiparticle linewidth [15, 20]. The spectral function used in the simulation takes the following form:

$$A(\mathbf{k}, \omega) = \frac{E_{\mathbf{k}} + \epsilon_{\mathbf{k}}}{\sqrt{8\pi\sigma E_{\mathbf{k}}}} e^{-\frac{(\omega+E_{\mathbf{k}})^2}{2\sigma^2}} + \frac{E_{\mathbf{k}} - \epsilon_{\mathbf{k}}}{\sqrt{8\pi\sigma E_{\mathbf{k}}}} e^{-\frac{(\omega-E_{\mathbf{k}})^2}{2\sigma^2}}, \quad (1)$$

where $E_{\mathbf{k}} = \sqrt{\epsilon_{\mathbf{k}}^2 + \Delta_{\mathbf{k}}^2}$ is the Bogoliubov quasiparticle dispersion. The superconducting gap $\Delta_{\mathbf{k}}$ has the following approximated temperature dependence:

$$\Delta_{\mathbf{k}}(T) = \Delta_{\mathbf{k}}(0) \tanh\left(2.34\sqrt{T_{\text{gap}}/T - 1}\right). \quad (2)$$

States between T_c and T_{gap} are labeled as fluc-SC. The quasiparticle width $\sigma(T)$ is modelled by a rounded step function plus a Fermi liquid self energy that mimics realistic experimental values in units of eV and Kelvin:

$$\sigma(T) = 0.028 + 5.56 \times 10^{-7} T^2 + 0.01 \tanh[5(T/T_c - 1)] + 5\omega^2. \quad (3)$$

Energy-momentum resolution is treated as a 2D Gaussian convolution on the 2D spectral function, where the momentum resolution is taken as the typical 10-pixel size. The background is treated as 10 times the average per-pixel intensity across the simulated cut multiplied by the Fermi function, which mimics the momentum-scrambling secondary scattering process in photoemission. Since we are mostly in intermediate to high count rate regime, the noise distribution is approximated as a Gaussian with a standard deviation of $\alpha\sqrt{N_{ij}}$, where N_{ij} is the simulated count at pixel $\{i, j\}$, and α is an input parameter to control the signal to noise ratio. This approximation

mimics the Poisson noise observed in real experiments, which is generally in the high-count-rate regime and asymptotically approaches a Gaussian noise. The entire spectrum takes an absolute value to eliminate negative counts due to the application of Gaussian noise at extremely low count regimes, which has negligible impact on the main spectral region of interest. A comparison of the parameter space of simulated and experimental data can be found in Supplementary Note 4. A total of 1,745 simulated spectra were obtained, with 80% (1,395) being utilized as training data.

B. Domain adaptation

DANN is a domain adaptation technique designed to reduce the domain distribution shift between the source (simulated) and target (experimental) domains. The model architecture comprises three parts as shown in Fig. 2: the feature extractor ($G_f(\cdot; \theta_f)$) with parameters θ_f , the label predictor ($G_y(\cdot; \theta_y)$) with parameters θ_y , and the domain classifier ($G_d(\cdot; \theta_d)$) with parameters θ_d . Training DANN involves minimizing the classification loss of the class classifier using labels from the source domain while simultaneously maximizing the error of the domain classifier using a gradient reversal layer (GRL) (denoted as $\mathcal{R}(\cdot)$). We define the \mathcal{L}_y and \mathcal{L}_d as the corresponding cross-entropy loss [31] of label prediction and domain classification. The GRL acts as an identity transformation during forward propagation and flips the sign of $\partial \mathcal{L}_d / \partial \theta_f$ during backpropagation. The training objective is formulated as follows:

$$\begin{aligned} E(\theta_f, \theta_y, \theta_d) = & \mathbb{E}_{(\mathbf{x}_i^s, y_i^s) \sim \mathcal{D}_s} \mathcal{L}_y(G_y(G_f(\mathbf{x}_i^s; \theta_f); \theta_y), y_i^s) \\ & - \lambda \left(\mathbb{E}_{\mathbf{x}_i^s \sim \mathcal{D}_s} \mathcal{L}_d(G_d(\mathcal{R}(G_f(\mathbf{x}_i^s; \theta_f)); \theta_d), d^s) \right. \\ & \left. + \mathbb{E}_{\mathbf{x}_j^t \sim \mathcal{D}_t} \mathcal{L}_d(G_d(\mathcal{R}(G_f(\mathbf{x}_j^t; \theta_f)); \theta_d), d^t) \right), \end{aligned} \quad (4)$$

where \mathbb{E} represents the expected value of the set; \mathbf{x}_i^s denotes a simulated spectrum with phase label y_i^s from the source domain $D_s = \{(\mathbf{x}_i^s, y_i^s)\}_{i=1}^{n_s}$; \mathbf{x}_j^t denotes an experimental spectrum in the target domain $D_t = \{(\mathbf{x}_j^t)\}_{j=1}^{n_t}$; d^s and d^t are the domain labels. Here, λ is the adaptation parameter, balancing the two objectives that shape the features during training. Upon training completion, the label predictor is capable of predicting labels for both source and target domain samples.

C. Model architecture and implementation

Our optimized model employs four convolutional layers with hidden channels of 16, 32, 64, and 64, respectively. Each layer utilizes a 3×3 convolutional kernel, a stride of 1, and padding of 2, followed by max pooling with the same kernel size and a stride of 2, and an activation function. All the activation functions used in this

network are rectified linear units (ReLU) except for the first convolutional layer. To alleviate the dying ReLU problem where some neurons become permanently inactive and only output 0 for any input during training, the first convolutional layer ReLU was replaced with the leaky ReLU (LeakyReLU) [32] using a default constant slope of 0.01. Post-convolution, the network applies adaptive average pooling to the feature maps, which are then flattened to interface with the subsequent fully connected layers. The domain classifier and label predictor are both two-layer fully connected neural networks with 64 hidden dimensions each. All models are implemented using PyTorch 1.12.1. The optimized training procedure employs the Adam optimizer [33] with a learning rate of 0.0005, weight decay (L2 penalty, 0.001), and early stopping. Dropout with a probability of 0.4 is applied after the last convolutional layer and in every layer of each fully connected neural network. Training is performed with mini-batches of 4 spectra for 150 epochs. The adaptation parameter is set to be 1.2 and is gradually increased from 0 through:

$$\lambda = \frac{2}{1 + e^{-\gamma \cdot p}} - 1, \quad (5)$$

in the early stages of the training, to suppress noisy signals from the domain classifier. Here, γ is set to 10 without being optimized, and p represents the training progress linearly changing from 0 to 1.

D. Model evaluation and hyperparameter tuning

Evaluating the performance of an unsupervised domain adaptation (UDA) model is challenging due to the lack of the target domain labels [34–36]. As the domain classifier acts as a regularizer on CNN [19], we first optimize the CNN model without the domain classifier using simulated ARPES data (detailed in Supplementary Note 5). We then fine-tune the adaptation parameter based on the transfer score (TS) metrics [36], which evaluates the transferability and discriminability of the feature space. The TS is formulated as follows:

$$\mathcal{T} = \mathcal{H} + \frac{|\mathcal{M}|}{\ln K}. \quad (6)$$

Here, \mathcal{H} denotes the Hopkins statistic [37], which measures the clustering tendency of the feature representation in the target domain; \mathcal{M} denotes mutual information between the input and prediction in the target domain; K is the number of classes for the normalization purpose. To obtain the Hopkins statistic, we define \mathbf{f}_t as the feature embeddings of all target domain samples, which is given by $\mathbf{f}_t = [f_1, f_2, \dots, f_{n_t}]$, where $f_j = G_f(\mathbf{x}_j^t; \theta_f)$. From \mathbf{f}_t , we randomly sample $m = 0.05n_t$ data points [38] without replacement to generate a set R . Additionally, we generate a set U comprising m data points sampled from a uniform distribution bounded by the minimum and maximum values along each feature dimension of

\mathbf{f}_t . We then compute two distance measures: u_k , the distance of samples in U from their nearest neighbor in R , and w_k , the distance of samples in R from their nearest neighbor in R . The Hopkins statistic is then defined as:

$$\mathcal{H} = \frac{\sum_{k=1}^m u_k}{\sum_{k=1}^m u_k + \sum_{k=1}^m w_k} \quad (7)$$

The mutual information is defined as:

$$\mathcal{M} = H\left(\mathbb{E}_{\mathbf{x}_j^t \sim \mathcal{D}_t} G_y(G_f(\mathbf{x}_j^t; \theta_f); \theta_y)\right) - \mathbb{E}_{\mathbf{x}_j^t \sim \mathcal{D}_t} H(G_y(G_f(\mathbf{x}_j^t; \theta_f); \theta_y)), \quad (8)$$

where $H(\cdot)$ denotes the information entropy. The optimized model is then trained using the labeled simulated training set and all unlabeled experimental spectra. The model checkpoint with the best TS is collected for test set predictions.

E. Occlusion-based attribution

By moving the occluding patch along the energy axis, we quantify the saliency for each spectrum sample at energy level $\omega = \nu$ as:

$$S_{\text{SC}}(\nu) = \max\left\{0, \bar{p}_{\text{SC}}[A(\mathbf{k}, \omega)] - \bar{p}_{\text{SC}}[\tilde{A}(\mathbf{k}, \omega; \nu)]\right\}, \quad (9)$$

where the occluded spectrum of the original spectrum $A(\mathbf{k}, \omega)$, with respect to a single baseline spectrum (A_0) at energy ν , is defined as

$$\tilde{A}(\mathbf{k}, \omega; \nu) = A(\mathbf{k}, \omega) + \delta(\omega - \nu)[A_0(\mathbf{k}, \nu) - A(\mathbf{k}, \nu)]. \quad (10)$$

Here, $\bar{p}_{\text{SC}}[\cdot]$ represents the ML model mapping from an input ARPES spectrum to the predicted SC probability \bar{p}_{SC} . Since we focus on features with positive contributions, a ReLU function is applied to filter out the distraction of negative values. Following recent feature attribution studies [39, 40], we choose various occlusion baselines to ensure robust explanation performance across different pixel intensities (see details in Supplementary Note 6).

-
- [1] G. Mahan, *Theory of Photoemission in Simple Metals*, Phys. Rev. B **2**, 4334 (1970).
- [2] J. A. Sobota, Y. He, and Z.-X. Shen, *Angle-Resolved Photoemission Studies of Quantum Materials*, Rev. Mod. Phys. **93**, 025006 (2021).
- [3] A. Damascelli, Z. Hussain, and Z.-X. Shen, *Angle-Resolved Photoemission Studies of the Cuprate Superconductors*, Rev. Mod. Phys. **75**, 473 (2003).
- [4] B. Keimer, S. Kivelson, M. Norman, S. Uchida, and J. Zaanen, *From Quantum Matter to High-Temperature Superconductivity in Copper Oxides*, Nature **518**, 179 (2015).
- [5] T. Kondo, W. Malaeb, Y. Ishida, T. Sasagawa, H. Sakamoto, T. Takeuchi, T. Tohyama, and S. Shin, *Point Nodes Persisting Far Beyond T_c in Bi2212* , Nat. Commun. **6**, 7699 (2015).
- [6] B. D. Faeth, S. Yang, J. K. Kawasaki, J. N. Nelson, P. Mishra, L. Chen, D. G. Schlom, and K. M. Shen, *Incoherent Cooper Pairing and Pseudogap Behavior in Single-Layer $\text{FeSe}/\text{SrTiO}_3$* , Phys. Rev. X **11**, 021054 (2021).
- [7] Y. Xu, H. Rong, Q. Wang, D. Wu, Y. Hu, Y. Cai, Q. Gao, H. Yan, C. Li, C. Yin, H. Chen, J. Huang, Z. Zhu, Y. Huang, G. Liu, Z. Xu, Z. Lin, and X. J. Zhou, *Spectroscopic Evidence of Superconductivity Pairing at 83 K in Single-Layer $\text{FeSe}/\text{SrTiO}_3$ Films*, Nat. Commun. **12**, 2840 (2021).
- [8] Y. He, S.-D. Chen, Z.-X. Li, D. Zhao, D. Song, Y. Yoshida, H. Eisaki, T. Wu, X.-H. Chen, D.-H. Lu, C. Meingast, T. P. Devereaux, R. J. Birgeneau, M. Hashimoto, D.-H. Lee, and Z.-X. Shen, *Superconducting Fluctuations in Overdoped $\text{Bi}_2\text{Sr}_2\text{CaCu}_2\text{O}_{8+\delta}$* , Phys. Rev. X **11**, 031068 (2021).
- [9] C. Chen, X. Chen, W. Tang, Z. Li, S. Wang, S. Ding, Z. Kang, C. Jozwiak, A. Bostwick, E. Rotenberg, M. Hashimoto, D. Lu, J. P. C. Ruff, S. G. Louie, R. J. Birgeneau, Y. Chen, Y. Wang, and Y. He, *Role of Electron-Phonon Coupling in Excitonic Insulator Candidate Ta_2NiSe_5* , Phys. Rev. Res. **5**, 043089 (2023).
- [10] Y. Wang, M. Claassen, C. D. Pemmaraju, C. Jia, B. Moritz, and T. P. Devereaux, *Theoretical Understanding of Photon Spectroscopies in Correlated Materials In and Out of Equilibrium*, Nat. Rev. Mater. **3**, 312 (2018).
- [11] A. Zong, B. R. Nebgen, S.-C. Lin, J. A. Spies, and M. Zuerch, *Emerging Ultrafast Techniques for Studying Quantum Materials*, Nat. Rev. Mater. **8**, 224 (2023).
- [12] J. Lee, F. Schmitt, R. Moore, S. Johnston, Y.-T. Cui, W. Li, M. Yi, Z. Liu, M. Hashimoto, Y. Zhang, D. Lu, T. P. Devereaux, D.-H. Lee, and Z.-X. Shen, *Interfacial Mode Coupling as the Origin of the Enhancement of T_c in FeSe Films on SrTiO_3* , Nature **515**, 245 (2014).
- [13] Q.-Y. Wang, Z. Li, W.-H. Zhang, Z.-C. Zhang, J.-S. Zhang, W. Li, H. Ding, Y.-B. Ou, P. Deng, K. Chang, et al., *Interface-Induced High-Temperature Superconductivity in Single Unit-Cell FeSe Films on SrTiO_3* , Chin. Phys. Lett. **29**, 037402 (2012).
- [14] T. Yilmaz, E. Vescovo, J. Sadowski, and B. Sinkovic, *Spectroscopic Evidence of Highly Correlated Electrons in VSe_2* , Phys. Rev. B **105**, 245114 (2022).
- [15] S.-D. Chen, M. Hashimoto, Y. He, D. Song, J.-F. He, Y.-F. Li, S. Ishida, H. Eisaki, J. Zaanen, T. P. Devereaux, et al., *Unconventional Spectral Signature of T_c in a Pure d -Wave Superconductor*, Nature **601**, 562 (2022).
- [16] D. Cho, K. Bastiaans, D. Chatzopoulos, G. Gu, and M. Allan, *A Strongly Inhomogeneous Superfluid in an Iron-Based Superconductor*, Nature **571**, 541 (2019).

- [17] K. Fagnan, Y. Nashed, G. Perdue, D. Ratner, A. Shankar, and S. Yoo, *Data and Models: A Framework for Advancing AI in Science*, Tech. Rep. (USDOE Office of Science (SC)(United States), 2019).
- [18] D. Ratner, B. Sumpter, F. Alexander, J. J. Billings, R. Coffee, S. Cousineau, P. Denes, M. Doucet, I. Foster, A. Hexemer, *et al.*, *BES Roundtable on Producing and Managing Large Scientific Data with Artificial Intelligence and Machine Learning*, DOESC Office of Basic Energy Sciences, Tech. Rep. (2019).
- [19] Y. Ganin, E. Ustinova, H. Ajakan, P. Germain, H. Larochelle, F. Laviolette, M. March, and V. Lempit-sky, *Domain-Adversarial Training of Neural Networks*, *J. Mach. Learn. Res.* **17**, 1 (2016).
- [20] Y. He, M. Hashimoto, D. Song, S.-D. Chen, J. He, I. Vishik, B. Moritz, D.-H. Lee, N. Nagaosa, J. Zaanen, T. P. Devereaux, Y. Yoshida, H. Eisaki, D. H. Lu, and Z.-X. Shen, *Rapid Change of Superconductivity and Electron-Phonon Coupling through Critical Doping in Bi-2212*, *Science* **362**, 62 (2018).
- [21] L. van der Maaten and G. Hinton, *Visualizing Data Using t-SNE*, *J. Mach. Learn. Res.* **9**, 2579 (2008).
- [22] D. Smilkov, N. Thorat, B. Kim, F. Viégas, and M. Wattenberg, *Smoothgrad: Removing Noise by Adding Noise*, arXiv:1706.03825 (2017).
- [23] F. Boschini, E. da Silva Neto, E. Razzoli, M. Zonno, S. Peli, R. Day, M. Michiardi, M. Schneider, B. Zwartsenberg, P. Nigge, *et al.*, *Collapse of Superconductivity in Cuprates Via Ultrafast Quenching of Phase Coherence*, *Nat. Mater.* **17**, 416 (2018).
- [24] X. Yang, C. Vaswani, C. Sundahl, M. Mootz, P. Gagel, L. Luo, J. Kang, P. Orth, I. Perakis, C. Eom, *et al.*, *Terahertz-Light Quantum Tuning of a Metastable Emergent Phase Hidden by Superconductivity*, *Nat. Mater.* **17**, 586 (2018).
- [25] Z. Sun and A. J. Millis, *Transient Trapping into Metastable States in Systems with Competing Orders*, *Phys. Rev. X* **10**, 021028 (2020).
- [26] S. Bozinovski, *Reminder of the First Paper on Transfer Learning in Neural Networks, 1976*, *Informatica* **44** (2020).
- [27] L. Y. Pratt, *Discriminability-Based Transfer Between Neural Networks*, *Adv. Neural Inf. Process. Syst.* **5** (1992).
- [28] S. Ben-David, J. Blitzer, K. Crammer, A. Kulesza, F. Pereira, and J. W. Vaughan, *A Theory of Learning from Different Domains*, *Mach. Learn.* **79**, 151 (2010).
- [29] H. Han and S. Choi, *Transfer Learning from Simulation to Experimental Data: NMR Chemical Shift Predictions*, *J. Phys. Chem. Lett.* **12**, 3662 (2021).
- [30] K. Yamada, C. H. Lee, K. Kurahashi, J. Wada, S. Wakimoto, S. Ueki, H. Kimura, Y. Endoh, S. Hosoya, G. Shirane, R. J. Birgeneau, M. Greven, M. A. Kastner, and Y. J. Kim, *Doping Dependence of the Spatially Modulated Dynamical Spin Correlations and the Superconducting-Transition Temperature in $La_{2-x}Sr_xCuO_4$* , *Phys. Rev. B* **57**, 6165 (1998).
- [31] I. Goodfellow, Y. Bengio, and A. Courville, *Deep Learning* (MIT Press, 2016).
- [32] A. L. Maas, A. Y. Hannun, A. Y. Ng, *et al.*, *Rectifier Nonlinearities Improve Neural Network Acoustic Models*, in *Proc. ICML*, Vol. 30 (Atlanta, GA, 2013) p. 3.
- [33] D. P. Kingma and J. Ba, *Adam: A Method for Stochastic Optimization*, arXiv:1412.6980 (2014).
- [34] P. Morerio, J. Cavazza, and V. Murino, *Minimal-Entropy Correlation Alignment for Unsupervised Deep Domain Adaptation*, arXiv:1711.10288 (2017).
- [35] K. Saito, D. Kim, P. Teterwak, S. Sclaroff, T. Darrell, and K. Saenko, *Tune It the Right Way: Unsupervised Validation of Domain Adaptation via Soft Neighborhood Density*, in *Proceedings of the IEEE/CVF International Conference on Computer Vision* (2021) pp. 9184–9193.
- [36] J. Yang, H. Qian, Y. Xu, and L. Xie, *Can We Evaluate Domain Adaptation Models Without Target-Domain Labels? A Metric for Unsupervised Evaluation of Domain Adaptation*, arXiv:2305.18712 (2023).
- [37] A. Banerjee and R. N. Dave, *Validating Clusters Using the Hopkins Statistic*, in *2004 IEEE International Conference on Fuzzy Systems (IEEE Cat. No. 04CH37542)*, Vol. 1 (IEEE, 2004) pp. 149–153.
- [38] R. G. Lawson and P. C. Jurs, *New Index for Clustering Tendency and Its Application to Chemical Problems*, *J. Chem. Inf. Comput. Sci.* **30**, 36 (1990).
- [39] P. Sturmfels, S. Lundberg, and S.-I. Lee, *Visualizing the Impact of Feature Attribution Baselines*, *Distill* (2020).
- [40] G. Erion, J. D. Janizek, P. Sturmfels, S. M. Lundberg, and S.-I. Lee, *Learning Explainable Models Using Attribution Priors* (2020).

ACKNOWLEDGEMENTS

We thank Mingda Li for insightful discussions. X.C., Y.S., and Y.W. acknowledge support from the Air Force Office of Scientific Research Young Investigator Program under grant FA9550-23-1-0153. Y.H. acknowledges support from NSF CAREER award No. DMR-2239171. J.Y. was partially supported by a seed fund from the Yale Provost’s Office. This research used resources of the National Energy Research Scientific Computing Center, a DOE Office of Science User Facility supported by the Office of Science of the U.S. Department of Energy under Contract No. DE-AC02-05CH11231 using NERSC award BES-ERCAP0023181.

AUTHOR CONTRIBUTIONS

Y.W., F.L., and Y.H. conceived the project. Y.H. and J.Y. prepared the dataset. X.C., Y.S., and E.H. built the ML model and carried out data analysis with the help of V.D. All the authors contributed to the interpretation of the results and the manuscript writing.

COMPETING INTERESTS

The authors declare no competing interests.